ChemComm

COMMUNICATION

View Article Online
View Journal | View Issue

Cite this: *Chem. Commun.*, 2023, 59, 3083

Received 9th December 2022,
Accepted 14th February 2023

DOI: 10.1039/d2cc06721h

rsc.li/chemcomm

Axisymmetric bis-tridentate Ir(III) photoredox catalysts for anticancer phototherapy under hypoxia†

Li Wei,[a] Rajesh Kushwaha,[b] Anyi Dao,[a] Zhongxian Fan,[ac] Samya Banerjee[b] and Huaiyi Huang *[a]

A novel axisymmetric bis-tridentate Ir(III) photocatalyst (Ir3) with synergetic type I/II photosensitization and photocatalytic activity was reported. Ir3 exhibited high photocytotoxicity toward drug-resistant cancer cells under normoxia and hypoxia. The photoactivated anticancer mechanism of Ir3 were investigated in detail. Overall, this new photo-redox catalyst can overcome hypoxia and drug resistance-related problems in clinical anticancer therapy.

Cancer remains one of the major health issues worldwide.[1] Although various cancer treatments are used in clinics, the side effects and drug resistance are the major concerns.[2] Thus, novel anticancer agents are urgently needed. Photodynamic therapy (PDT) which offers spatiotemporal control over the drug activation, has shown great potential to overcome the drawbacks of chemotherapy.[3] PDT normally uses light to excite a photosensitizer (PS) to generate an anticancer response *via* reactive oxygen species (ROS) production.[4] However, due to the ROS-dependent anticancer mechanism, PDT has limited scope against hypoxic tumors.[5]

Recently, the concept of in-cell photocatalysis has emerged to improve the efficiency of cancer phototherapy.[6] In this newly developed research field, photocatalysts have been applied to catalytically oxidize cellular coenzyme I, the reduced nicotinamide dinucleotide (NADH), to its oxidized form (NAD^+) upon light irradiation.[7] NADH plays an essential role in the mitochondrial tricarboxylic acid cycle, glycolysis, redox balance, and as a coenzyme for >400 oxidoreductases. Importantly, NADH functions as the primary electron source in the mitochondrial electron transport (ETC) chain.[8] The ROS released from ETC under hypoxia has been discovered to support the survival and development of cancer cells.[9] Thus, photo-catalytic depletion of NADH and the dysfunction of ETC provide a multi-targeting anticancer mechanism of action under hypoxia.

Previously, we reported terpyridyl-Ir(III) complexes of the type $[Ir(N^N^N)(C^N)Cl]^+$ as metal photocatalysts to induce NADH photocatalysis in cancer cells.[10] However, the chloride ligand may undergo hydrolysis, similar to cisplatin. Moreover, the existence of stereoisomers may also bring unanticipated side effects.[11] Unlike many octahedral tris-bidentate species, bis-tridentate metal complexes are achiral with appealing axial symmetry.[12] However, the majority of bis-tridentate polypyridyl metal complexes suffer from show poor photophysical properties due to distortion of the crystal field.[13] Thus the PDT application of bis-tridentate metal complexes is seldom reported compared with those of tris-bidentate systems.[14]

The potential threat of the stereoisomers encourages us to optimize the structural design of metal photocatalysts based on the structural diversity and nature of the coordination system. Herein, we reported the rational design of two types of axisymmetric bis-tridentate Ir(III) photocatalysts (**Ir1–Ir3**, Scheme 1)

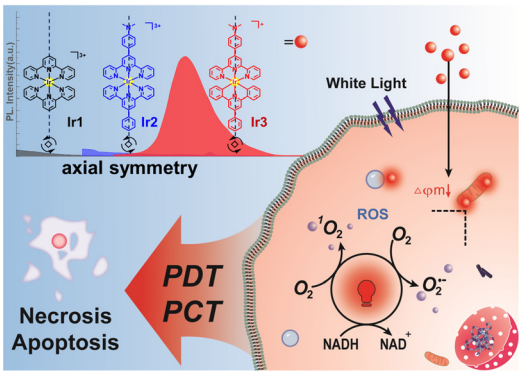

Scheme 1 Synergistic anticancer phototherapy with axisymmetric bis-tridentate Ir(III) photocatalysts.

[a] *School of pharmaceutical Sciences (Shenzhen), Shenzhen Campus of Sun Yat-sen University, Sun Yat-sen University, Shenzhen, 518107, P. R. China. E-mail: huanghy87@mail.sysu.edu.cn*

[b] *Department of Chemistry, Indian Institute of Technology (BHU), Varanasi, UP-221005, India*

[c] *Shenshan Medical Center, Memorial Hospital of Sun Yat-Sen University, China*

† Electronic supplementary information (ESI) available. See DOI: https://doi.org/10.1039/d2cc06721h

and investigated the potent phototherapeutic activity toward drug-resistant cancer cells under normoxia and hypoxia. Polypyridyl Ir(III) complexes such as $[Ir(tpy)_2]^{3+}$ (**Ir1**, tpy = [2,2′:6′,2″-terpyridin]) normally do not exhibit intense visible absorptions.[13] Thus, dimethylamine was introduced as the auxochrome to construct the symmetrical tridentate N^N^N ligand 4-([2,2′:6′,2″-terpyridin]-4′-yl)-*N*,*N*-dimethylaniline (**Ir2**) to enhance the light absorption property at a longer wavelength.[15] According to our previous work,[10] we assumed that cyclometallation can improve the photophysical properties of bis-tridentate Ir(III) photocatalyst. Thus the symmetrical C^N^C ligand 2,4,6-triphenylpyridine was also designed to construct the axisymmetric cyclometalated Ir(III) photocatalyst (**Ir3**) for comparative study with **Ir2**.

The synthetic routes of the tridentate ligands and Ir(III) photocatalysts were shown in the supporting information. The synthesis of **Ir1–Ir3** required harsh reaction conditions (200 °C) to overcome the inertness of the coordination sphere. The Ir(III) complexes were characterized by nuclear magnetic resonance and high resolution mass spectrometry (Fig. S1–S6, ESI†). It was found that the cyclometalated photocatalyst **Ir3** (+ 0.26) exhibited a much higher log *P* value than the polypyridyl photocatalysts **Ir1** (−0.33) and **Ir2** (−0.44) (Fig. 1a and Table. S1, ESI†).

The photophysical properties of **Ir1–Ir3** were investigated in various solvents to verify the influence of solvent polarity and viscosity. **Ir2** exhibited much extended absorption tailing to 700 nm than **Ir1** (Fig. 1a and Fig. S7, ESI†). Due to the cyclometalation effect, **Ir3** showed a significant blue-shift absorption compared with **Ir2**. **Ir1** and **Ir2** did not emit phosphorescence at room temperature (Fig. 1a and Fig. S8, ESI†). In contrast, **Ir3** exhibited broad and intense phosphorescence between 600–800 nm in CH_2Cl_2 according to the 3D mapping results (Fig. 1b). The phosphorescence quantum yield of **Ir3** was around 1% (Table S1, ESI†). In addition, the emission intensity of **Ir3** enhanced significantly in low polarity (CH_2Cl_2) and high viscosity solvent (ethylene glycol) (Fig. S8, ESI†). Moreover, the excited state lifetimes (Fig. 1c) and phosphorescence intensity (Fig. 1d and Fig. S9, ESI†) of **Ir3** increased in nitrogen-saturated solution compared with that in aerated solution. This result indicates that **Ir3** at the excited state can interact with molecular oxygen.

Furthermore, to rationalize the photophysical properties of **Ir2** and **Ir3**, the computational studies of the complexes (**Ir2–Ir3**) were studied in cationic form by density functional theory (DFT) using the Gaussian 16 quantum chemistry package.[16] The LANL2DZ basis set for Ir and the 6-31g basis set for all other atoms with the B3LYP function, were employed for geometry optimization during calculations. The energy-optimized structures of **Ir2–Ir3** showed a distorted octahedral geometry (Fig. S10, ESI†). For **Ir2**, the lowest unoccupied molecular orbital (LUMO) resided on the orbital of the auxochrome containing phenyl terpyridine and the highest occupied molecular orbital (HOMO) was on the phenyl terpyridine moiety (Fig. S10, ESI†). But in the case of **Ir3**, the HOMO was localized close to the metal center on auxochrome containing phenyl terpyridine, while LUMO was localized far from the metal center on auxochrome containing phenyl terpyridine (Fig. S10, ESI†). The cyclometallation effect of **Ir3** significantly reduced the energy of both HOMO and LUMO as compared to **Ir2** which depicted the better electron accepting ability of **Ir3** than **Ir2**. However, the HOMO–LUMO energy gap **Ir3** (2.52 eV) was higher than **Ir2** (1.52 eV). The UV-Vis absorption and singlet excited state energy levels calculations were also conducted by time-dependent DFT.[16] The calculated UV-vis spectra (singlet excited state, $S_0 \rightarrow S_n$ transition) were found to be in accordance with the experimental data (Fig. 1a and Table S2, ESI†). The $S_0 \rightarrow S_1$ transition state of **Ir3** (2.03 eV, f = 0.0132) (Table S2, ESI†) may be ascribed to metal to ligand charge transfer.

The high dark- and light-stability are essential for potent photosensitizers to avoid dark toxicity and photo-decomposition. The light stability test in Dulbecco's modified eagle medium (DMEM) confirmed the excellent photo-stability of **Ir1–Ir3** since the UV-Vis spectra changed slightly (Fig. S11, ESI†). In addition, **Ir3** exhibited excellent long term dark- and photo-stability in DMSO as tracked by ^{1}H NMR (Fig. S12, ESI†).

The high stability and oxygen sensitive phosphorescence of **Ir3** inspired us to investigate the photosensitization activity. Upon light excitation, photosensitizers can generate singlet oxygen ($^1O_2$) *via* a type II energy transfer pathway.[4] We used 9,10-anthracenediyl-bis(methylene) dimalonic acid (ABDA) to detect the $^1O_2$ production efficacy. In the dark, the absorbance of ABDA remained unchanged in the presence of **Ir1–Ir3** (Fig. S13, ESI†). Upon light irradiation, **Ir3** was more effective to decreased the absorption of ABDA than **Ir1** and **Ir2**, indicating a stronger $^1O_2$ generation ability of **Ir3** (Fig. 2a and Fig. S13–S15, ESI†).

Recently, in-cell photoredox catalysis of NADH *via* excited state single electron transfer pathway has been recognized as a novel mechanism action to combat cancer cells.[10] NADH is the

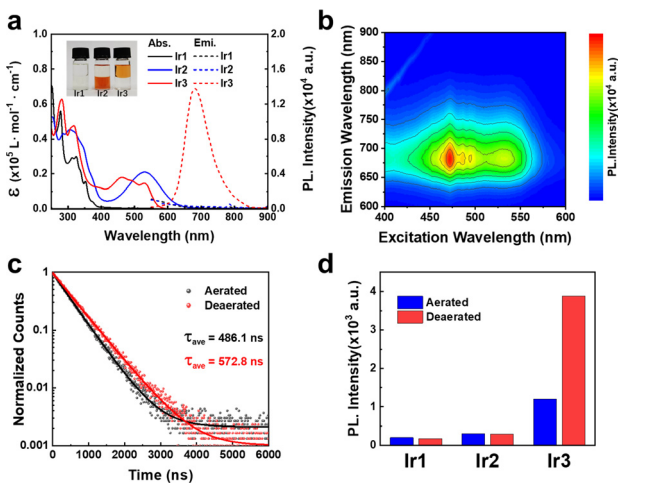

Fig. 1 (a) UV-Vis absorption and emission spectra of **Ir1–Ir3** in CH_2Cl_2 at room temperature. Insert: Log $P_{o/w}$ of **Ir1–Ir3** (b) 3D mapping phosphorescence spectra of the **Ir3** (10 μM) in CH_2Cl_2 at room temperature. (c) Phosphorescence lifetime of **Ir3** in CH_2Cl_2 under air or N_2. (d) Phosphorescence intensity of **Ir1–Ir3** (10 μM) in CH_2Cl_2.

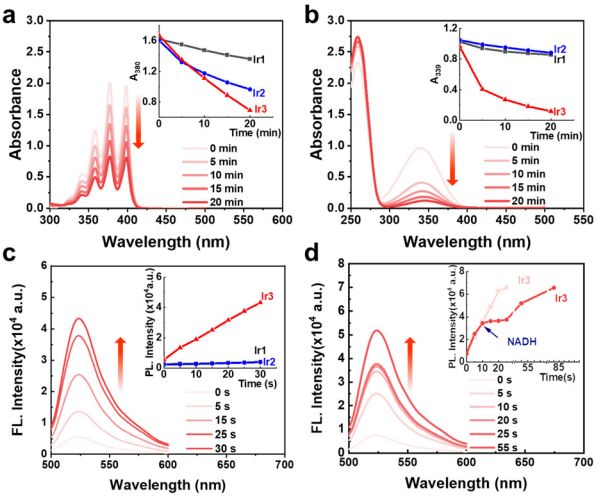

Fig. 2 Photoactivity of **Ir1–Ir3** (5 μM) under white light (14.3 mW cm^{-2}) irradiation. (a) $^1O_2$ generation efficiency of **Ir1–Ir3** detected by ABDA (200 μM). (b) Photocatalytic oxidation of NADH (160 μM) by **Ir1–Ir3**. $O_2^{\bullet-}$ generation efficiency of **Ir1–Ir3** detected by DHR123 (5 μM). (d) $O_2^{\bullet-}$ generation efficiency of **Ir3** in the presence of NADH (5 μM).

electron source of mitochondrial ETC thus NADH depletion will damage the hypoxic homeostasis of cancer cell.[9] The NADH photocatalytic activities of **Ir1–Ir3** were detected by UV-Visible spectroscopy. In the dark, **Ir1–Ir3** (5 μM) didn't change the absorption spectra of NADH (160 μM) after 20 min incubation (Fig. S16, ESI†). In contrast, upon irradiation (white light, 14.3 mW cm^{-2}), **Ir3** dramatically decreased the absorbance of NADH (Fig. 2b). The turnover frequency (TOF) of **Ir3** reached 214 h^{-1} (Fig. S17, ESI†) which was two times higher the terpyridyl-based Ir(III) photocatalyst reported before.[10] Moreover, **Ir3** can also photocatalyse cytochrome *c* (cyt *c*) reduction in the presence of NADH. (Fig. S18, ESI†)

Since both photocatalysis and type I photosensitization use excited state electron transfer mechanism, the superoxide radical ($O_2^{\bullet-}$) generation activity of **Ir1–Ir3** was also detected by dihydrorhodamine 123 (DHR123). In the dark, the absorbance of DHR123 did not change in the presence of **Ir1–Ir3** (Fig. S19, ESI†). Upon white light irradiation, **Ir3** (5 μM) enhanced the fluorescence intensity of DHR123 (5 μM) by nearly 5 times only after 30 seconds of white light irradiation (14.3 mW cm^{-2}) (Fig. 2c and Fig. S19, ESI†). However, the polypyridyl photocatalysts **Ir1** and **Ir2** were inactive under the same condition (Fig. S19, ESI†), indicating that cyclometallation can enhance the photochemical property of axisymmetric bis-tridentate Ir(III) complexes. Moreover, we tested the $O_2^{\bullet-}$ generation ability in the presence of low amount of NADH (5 μM). It was found that the fluorescence intensity of DHR123 remained unchanged during the photocatalysis of NADH by **Ir3** (Fig. 2d and Fig. S20, ESI†). Thus within cancer cells, the cellular substrates such as NADH may be superior to react with **Ir3** than oxygen, indicating low oxygen dependent mechanism of action. Overall, the above results revealed that **Ir3** could be used as both effective type I/II photosensitizer and photocatalyst.

Table 1 Dark- and photo-cytotoxicity of **Ir3**

Cell Line		A549 Normoxia	A549 Hypoxia	A549/DDP Normoxia	A549/DDP Hypoxia
Ir3	Dark[a]	$0.80^{\pm0.05}$	$3.85^{\pm1.08}$	$3.03^{\pm0.14}$	$9.39^{\pm0.68}$
	Light[b]	$0.0012^{\pm0.0002}$	$0.028^{\pm0.004}$	$0.0033^{\pm0.0003}$	$0.0082^{\pm0.0005}$
	PI[c]	666.7	137.5	918.1	1145.1
DDP[d]		$2.80^{\pm0.12}$	$3.58^{\pm0.25}$	$37.98^{\pm0.88}$	$69.23^{\pm1.24}$

Cell cytotoxicity tests were repeated triplicates. [a] 4 h drug exposure in the dark, replaced by fresh medium and followed by 44 h incubation. [b] The 4 h drug exposure in the dark, replaced by fresh medium and white light irradiation (17.2 J cm^{-2}) followed by 44 h incubation. [c] PI = IC_{50}(Dark)/IC_{50}(Light). [d] 48 h drug exposure.

The synergistic photosensitization and photocatalytic activity of **Ir3** promoted us to explore the anticancer phototherapy efficacy. The cisplatin sensitive A549 cell line and the cisplatin resistant cancer cell line A549/DDP under normoxia and hypoxia were tested. The clinical chemotherapy agent cisplatin was introduced as positive control. Cancer cells were exposed to diverse compounds respectively for 4 h and then replaced with fresh cell culture medium following by dark or white light treatment (17.2 J cm^{-2}) and 44 h recovery. The dark and light IC_{50} values were listed in Table 1 and Table S4 (ESI†). Under normoxia, the polypyridyl photocatalysts **Ir1–Ir2** exhibited both low dark and light cytotoxicity. The cyclometalated photocatalyst **Ir3** exhibited much promising dark- (IC_{50} = 0.80–3.03 μM) and nano molar photo-cytotoxicity (IC_{50} = 1.2–3.3 nM) toward both A549 and A549/DDP cancer cells. It's necessary to mention that the light cytotoxicity of **Ir3** was three orders of magnitude lower than the chemotherapeutic agent cisplatin. The high photo index of **Ir3** (667–918) under normoxia promoted us to further investigate the phototherapeutic activity under hypoxia (5% oxygen). Importantly, **Ir3** also exhibited high PI values (PI = 137–1145) toward both A549 and A549/DDP under hypoxia. Then we investigated the relative intracellular NADH levels of A549/DDP cells treated with **Ir3**. As shown in Fig. S21 (ESI†), the results revealed that the cellular NADH could be distinctly depleted. Thus, **Ir3** was highly active, due to the effective in-cell photocatalysis activity of NADH, toward sensitive and drug-resistant cancer cells under both normoxia and hypoxia. This finding is highly important considering that the anticancer phototherapy activity of photosensitizers used in clinic are limited by the hypoxic tumor microenvironment.

The phosphorescent nature of **Ir3** inspired us to investigate the cellular localization. **Ir3** can penetrate into the A549/DDP cells and localized mainly at the mitochondria rather than lysosome (Fig. 3a). Mitochondria play an important role in cellular energy production as well as cell survival under hypoxia.[17] Thus the mitochondria targeting nature of **Ir3** may result in the high dark- and photo-cytotoxicity under both normoxia and hypoxia.

The intracellular ROS generation ability of **Ir3** was also detected. As shown in Fig. 3b and Fig. S22 (ESI†), A549/DDP cells pretreated with **Ir3** did not emit green 2′,7′-dichlorofluorescein (DCF) signals.[7b] Upon white light irradiation (irradiance: 17.2 J cm^{-2}), the intracellular DCF signal enhanced significantly,

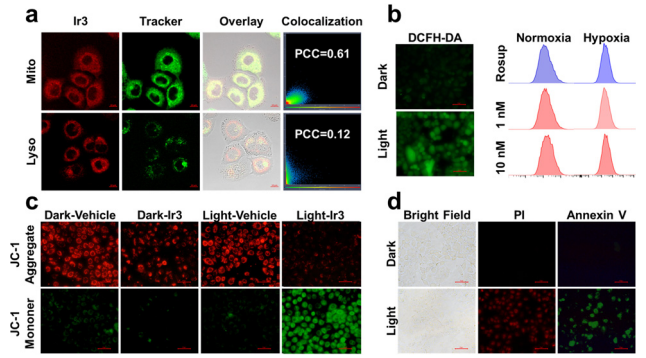

Fig. 3 Cellular response induced by **Ir3** after white light irradiation (17.2 J cm^{-2}). (a) Cellular localization of **Ir3** (1 μM) in A549/DDP cells co-staining with mitotracker and lysotracker dyes (100 nM). Scale bar: 10 μm. (b) Fluorescence imaging of intracellular generation of reactive oxygen species in A549/DDP cells induced by **Ir3** (0.2 μM) and flow cytometry examination under different condition. Rosup (5 mg mL^{-1}) as positive control. scale bar: 50 μm. (c) Mitochondrial membrane potential change in A549/DDP cells induced by **Ir3** (0.2 μM), scale bar: 50 μm. (d) Photo-induced necro-apoptotic death of A549/DDP cells by **Ir3** scale bar: 50 μm.

indicating intracellular production of ROS within A549/DDP cells. To verify the ROS species generated by **Ir3**, A549/DDP cells were stained with singlet oxygen sensor green (SOSG) or dihydroethidium (DHE) probe, respectively.[7b] Similarly, the green fluorescence of SOSG and red fluorescence of DHE enhanced significantly within cancer cells only after light irradiation (Fig. S23 and S24, ESI†), indicating singlet oxygen and superoxide anion were generated within A549/DDP cancer cells.

Since **Ir3** can target mitochondria and induce cancer cell death, tetraethylbenzimidazolylcarbocyanine iodide (JC-1) was applied to investigate the influence on mitochondrial membrane potential (MMP).[10b] Upon light irradiation, the green signal of JC-1 enhanced while the red signal decreased readily as evidence of MMP depletion and mitochondrial damage (Fig. 3c and Fig. S25, ESI†). The disruption of MMP has been recognized as a sign of cell apoptosis. Thus, annexin V-FITC/propidium iodide (PI)[10b] staining was conducted to identify the potent cell death mechanism. It was found that neither annexin V-FITC nor PI can stain the cells pretreated with **Ir3** (2 μM) in the dark. However, upon light irradiation, a great number of cells were stained by both annexin V-FITC and PI, revealing necroptosis cell death (Fig. 3d and Fig. S26, ESI†).

In summary, we compared two types of axisymmetric bis-tridentate Ir(III) photocatalysts for photocatalytic therapy towards drug resistant cancer cells under normoxia and hypoxia. The cyclometalated Ir(III) photocatalyst **Ir3** exhibited superior type I/II photosensitization and NADH photocatalytic activity than the polypyridyl Ir(III) photocatalysts **Ir1** and **Ir2**. **Ir3** located at mitochondria and showed strong photocytotoxicity toward cisplatin resistant cancer cells under both normoxia and hypoxia. Overall, we discovered that cyclometallation can significantly enhanced the in-cell photocatalysis efficiency of bis-tridentate Ir(III) photocatalysts and has the potential to solve the drug resistance and hypoxia problems in clinical anticancer therapy. However, long wavelength light excited metal photocatalysts with high biocompatibility are still to be developed to meet the requirement of clinical anticancer phototherapy.

We appreciate the financial support from the National Natural Science Foundation of China (NSFC 22277153, 22007104), Guangdong Basic and Applied Basic Research Foundation (2021B1515020050), the Fundamental Research Funds for the Central Universities (22lgqb37), the Science, Technology and Innovation Commission of Shenzhen Municipality (JCYJ20190807152616996), and SERB (SRG/2022/000030), the Government of India. R. Kushwaha thanks the Ministry of Education, the Government of India for the Prime Minister's Research Fellowship.

Conflicts of interest

The authors declare no conflict of interest.

References

1 H. Sung, J. Ferlay, R. Siegel, M. Laversanne, I. Soerjomataram, A. Jemal and F. Bray, *Ca-Cancer J. Clin.*, 2021, **71**, 209–249.
2 (*a*) S. Rottenberg, C. Disler and P. Perego, *Nat. Rev. Cancer*, 2021, **21**, 37–50; (*b*) N. Miltenburg and W. Boogerd, *Cancer Treat. Rev.*, 2014, **40**, 872–882.
3 P. Lo, M. Rodríguez-Morgade, R. Pandey, D. Ng, T. Torres and F. Dumoulin, *Chem. Soc. Rev.*, 2020, **49**, 1041–1056.
4 (*a*) P. Agostinis, K. Berg, K. Cengel, T. Foster, A. Girotti, S. Gollnick, S. Hahn, M. Hamblin, A. Juzeniene, D. Kessel, M. Korbelik, J. Moan, P. Mroz, D. Nowis, J. Piette, B. Wilson and J. Golab, *Ca-Cancer J. Clin.*, 2011, **61**, 250–281; (*b*) L. Gourdon, K. Cariou and G. Gasser, *Chem. Soc. Rev.*, 2022, **51**, 1167–1195.
5 L. Huang, S. Zhao, J. Wu, L. Yu, N. Singh, K. Yang, M. Lan, P. Wang and J. Kim, *Coord. Chem. Rev.*, 2021, **438**, 213888.
6 M. Li, Y. Xu, Z. Pu, T. Xiong, H. Huang, S. Long, S. Son, L. Yu, N. Singh, Y. Tong, J. Sessler, X. Peng and J. Kim, *Proc. Natl. Acad. Sci. U.S.A.*, 2022, **119**, e2210504119.
7 (*a*) H. Huang, S. Banerjee, K. Qiu, P. Zhang, O. Blacque, T. Malcomson, M. Paterson, G. Clarkson, M. Staniforth, V. Stavros, G. Gasser, H. Chao and P. Sadler, *Nat. Chem.*, 2019, **11**, 1041–1048; (*b*) M. Li, K. Gebremedhin, D. Ma, Z. Pu, T. Xiong, Y. Xu, J. Kim and X. Peng, *J. Am. Chem. Soc.*, 2022, **144**, 163–173; (*c*) S. Qi, Z. Jin, Y. Jian, Y. Hou, C. Li, Y. Zhao, X. Wang and Q. Zhou, *Chem. Commun.*, 2021, **57**, 4162–4165.
8 A. Chiarugi, C. Dölle, R. Felici and M. Ziegler, *Nat. Rev. Cancer*, 2012, **12**, 741–752.
9 T. Klimova and N. Chandel, *Cell Death Differ.*, 2008, **15**, 660–666.
10 (*a*) C. Huang, C. Liang, T. Sadhukhan, S. Banerjee, Z. Fan, T. Li, Z. Zhu, P. Zhang, K. Raghavachari and H. Huang, *Angew. Chem., Int. Ed.*, 2021, **60**, 9474–9479; (*b*) Z. Fan, Y. Rong, T. Sadhukhan, S. Liang, W. Li, Z. Yuan, Z. Zhu, S. Guo, S. Ji, J. Wang, R. Kushwaha, S. Banerjee, K. Raghavachari and H. Huang, *Angew. Chem., Int. Ed.*, 2022, **61**, e202202098.
11 M. Franks, G. Macpherson and W. Figg, *Lancet*, 2004, **363**, 1802–1811.
12 E. Medlycott and G. Hanan, *Chem. Soc. Rev.*, 2005, **34**, 133–142.
13 E. Baranoff, J. Collin, L. Flamigni and J. Sauvage, *Chem. Soc. Rev.*, 2004, **33**, 147–155.
14 (*a*) R. Ryan, K. Stevens, R. Calabro, S. Parkin, J. Mahmoud, D. Kim, D. Heidary, E. Glazer and J. Selegue, *Inorg. Chem.*, 2020, **59**, 8882–8892; (*b*) S. Paul, P. Kundu, P. Kondaiah and A. Chakravarty, *Inorg. Chem.*, 2021, **60**, 16178–16193; (*c*) B. Liu, S. Monro, Z. Li, M. Jabed, D. Ramirez, C. Cameron, K. Colón, J. Roque, S. Kilina, J. Tian, S. McFarland and W. Sun, *ACS Appl. Bio Mater.*, 2019, **2**, 2964–2977.
15 J. Wang and G. Hanan, *Synlett*, 2005, 1251–1254.
16 S. Ji, W. Wu, W. Wu, H. Guo and J. Zhao, *Angew. Chem., Int. Ed.*, 2011, **50**, 1626–1629.
17 (*a*) S. Sabharwal and P. Schumacker, *Nat. Rev. Cancer*, 2014, **14**, 709–721; (*b*) D. Wallace, *Nat. Rev. Cancer*, 2012, **12**, 685–698.

